

centred on a f.c.c. lattice<sup>12</sup>. The molecular form factor  $f$  for this radial charge density  $U(r) = \rho\delta(r - r_c)$ , where  $\rho$  is the uniform charge distribution on the sphere, can be written as<sup>13</sup>

$$f(E) = \int_0^\infty \rho\delta(r - r_c) \frac{\sin\left(\frac{2\pi r}{d}\right)}{\left(\frac{2\pi r}{d}\right)} dr = \frac{\rho\epsilon \sin\left(\frac{2\pi r_c E}{\epsilon}\right)}{2\pi r_c E} \quad (1)$$

where the constant  $\epsilon \equiv Ed = hc/2 \sin \theta$ , with  $E$  the diffraction energy and  $d = a/\sqrt{h^2 + k^2 + l^2}$  the lattice spacing of the cubic-lattice  $hkl$  plane. Equation (1) has zeros at

$$\frac{a}{r_c} = \frac{2\sqrt{h^2 + k^2 + l^2}}{n} \quad (2)$$

with  $n$  an integer. For the atmospheric-pressure case<sup>7</sup>, where  $a_0 = 14.198 \text{ \AA}$ , the (200) peak will be absent for  $r_c = 3.55 \text{ \AA}$ , in close agreement with the experimentally<sup>7</sup> determined value of  $3.5 \text{ \AA}$  and the theoretical<sup>4</sup> value of  $3.55 \text{ \AA}$  for the free  $C_{60}$  molecule. If, however, the intramolecular bonds are significantly less compressible than the intermolecular bonding, then  $a/r_c$  will be pressure dependent, and the accidental absence of the (200) line will be eliminated at high pressure. This is shown in Fig. 3, where the (200) intensity increases as it shifts out of the region of  $f = 0$ . By 20 GPa, the (111) diffraction peak intensity has diminished nearly to zero. Although detailed analysis is complicated by powder orientation effects, these observed intensity changes imply a reduction in  $a/r_c$  of nearly 13% at 20 GPa. As  $a$  has diminished by more than 12% at this pressure, this implies no reduction in  $r_c$  within experimental error. This is consistent with the expected significantly lower compressibility of the  $C_{60}$  molecule relative to the bulk fullerite.

Figure 2 demonstrates that above about 5 GPa there are differences between hydrostatic and non-hydrostatic compression of solid  $C_{60}$ . These differences are not due to pressure gradients between the position of the ruby chip and the X-ray collimator position, as the pressure was measured at several places in the sample chamber. For example, a maximum gradient of 1 GPa over the entire sample was measured in experiment 2 at 18.7 GPa. In the geometry used here, the EDXD technique probes diffraction planes parallel to the stress axis of the diamond anvil cell. The existence of a higher stress in this direction will result in a larger measured lattice parameter and volume, determined by the Poisson ratio of fullerite. For this to explain the present data, the highly compressible fullerite must be capable of supporting uniaxial stresses. One possible mechanism for the required shear strength is the presence of elongated  $C_{70}$  molecules or other fullerenes in the lattice that act as dislocation pinning centres. Such an effect has been seen in graphite, where the basal-plane shear modulus  $c_{44}$  increases by nearly an order of magnitude when substitutionally doped with 1500 p.p.m. boron<sup>14</sup>. Further work, including diffraction-angle dependence of the measured lattice constant, is needed to confirm this explanation.

Both the  $C_{60}$  molecule and the f.c.c. fullerite structure are thus stable upon hydrostatic compression to at least 20 GPa. The non-hydrostatic experiments 2 and 3, however, show crystallographic transformations from the f.c.c. structure at  $20 \pm 2 \text{ GPa}$  and  $16.5 \pm 1.0 \text{ GPa}$ , respectively. The difference in measured transition pressures is probably due to differences in the details of the stress state achieved in the two experiments. In experiment 3, where no pressure medium was used, the transition is characterized by an abrupt splitting of the (111) diffraction peak, broadening of the (311) peak, and no influence on the (220) peak to 24 GPa. Such behaviour indicates a transition to a structure of lower symmetry. The transition was observed well after the ruby spectra indicated the presence of a non-hydrostatic state of stress. The high-pressure phase cannot be indexed to a hexagonally close-packed unit cell, and further work is needed to characterize this phase and its reversibility.

Received 3 May; accepted 10 May 1991.

1. Krättschmer, W., Lamb, L. D., Fostiropoulos, K. & Huffman, D. R. *Nature* **347**, 354–358 (1990).
2. Haddon, R. C. *et al.* *Nature* **350**, 320–322 (1991).
3. Hebard, A. F. *et al.* *Nature* **350**, 600–601 (1991).
4. Haddon, R. C., Brus, L. E. & Raghavachari, K. *Chem. Phys. Lett.* **131**, 165–169 (1986).
5. Hanfland, M., Beister, H. & Syassen, K. *Phys. Rev. B* **39**, 12589–12603 (1989).
6. Ruoff, R. S. & Ruoff, A. L. *Nature* **350**, 663–664 (1991).
7. Flemming, R. M. *et al.* *Proc. Mater. Res. Soc. Boston*, November, 1990 (Materials Research Society, Boston, 1991).
8. Mao, H. K., Bell, P. M., Shaner, J. W. & Steinberg, D. J. *J. appl. Phys.* **49**, 3276–3283 (1978).
9. Vinet, P., Ferrante, J., Smith, J. R. & Rose, J. H. *J. Phys. C* **19**, L467–L473 (1986).
10. Macdonald, J. R. & Powell, D. R. *J. Res. Natl Bur. Stand. A*, **75A**, 441–453 (1971).
11. Donohue, J. *The Structure of the Elements* (Wiley, New York, 1974).
12. Fischer, J. E. *et al.* *Science* (submitted).
13. James, R. W. *The Optical Principles of the Diffraction of X-rays* (Ox Bow, Woodbridge, Connecticut, 1982).
14. Soule, D. E. & Nezbeda, C. W. *J. appl. Phys.* **39**, 5122–5139 (1968).

ACKNOWLEDGEMENTS. This work is based upon data acquired at CHESS, supported by the NSF. We thank A. L. Ruoff for the use of his ruby system.

## Simulations of the effect of a warmer climate on atmospheric humidity

Anthony D. Del Genio, Andrew A. Lacis & Reto A. Ruedy

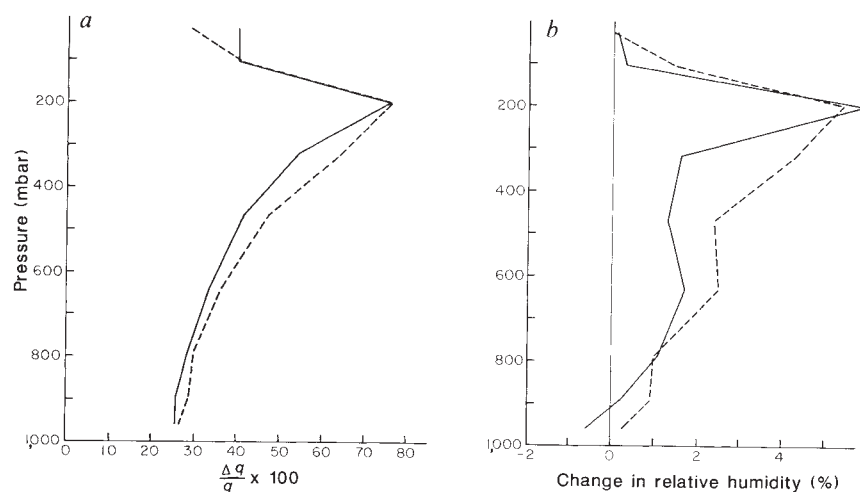
NASA/Goddard Institute for Space Studies, New York, New York 10025, USA

**THE increases in the concentration of water vapour constitute the single largest positive feedback in models of global climate warming caused by greenhouse gases<sup>1,2</sup>. It has been suggested<sup>3–5</sup> that sinking air in the regions surrounding deep cumulus clouds will dry the upper troposphere and eliminate or reverse the direction of water vapour feedback. We have now tested this hypothesis by performing an idealized simulation of climate change with two different versions of a climate model. The versions differ in their parameterizations of moist convection and stratiform clouds, but both incorporate the drying due to subsidence of clear air. Despite increased drying of the upper troposphere by cumulus clouds, upper-level humidity increases in the warmer climate because of enhanced upward moisture transport by the general circulation and increased accumulation of water vapour and ice at cumulus cloud tops. The model behaviour is consistent with recent satellite estimates of the water vapour feedback<sup>6,7</sup>.**

We express water vapour concentration in terms of the specific humidity  $q$ , defined as the ratio of the mass density of water vapour to that of moist air.  $q = q_s r$ , where  $q_s$ , the saturation humidity, is the maximum possible humidity in equilibrium over a flat surface of water, and  $r$ , the relative humidity, is the fraction of the saturation humidity actually realized.  $q_s$  is a function only of temperature and pressure and is determined by the Clausius–Clapeyron equation of thermodynamics<sup>8</sup>;  $r$  is the net result of competing dynamic, radiative and microphysical processes. The values of  $q_s$  increase nonlinearly with temperature. As a result, the  $q$  of near-surface tropical air is two to three orders of magnitude greater than that of the colder upper troposphere and polar regions.

Evaporation from the surface and precipitation are the ultimate source and sink of atmospheric moisture, respectively. Within the atmosphere, several processes redistribute water vapour vertically and horizontally. Deep precipitating cumulus-updrafts lift moisture from near the surface and inject some of it into the upper troposphere as vapour or ice, a process known as detrainment. The clear environment surrounding the updrafts slowly sinks in response; this compensating subsidence dries the atmosphere by bringing low- $q$  air down from above. Condensation in clouds is a local sink of water vapour, and re-evaporation of falling precipitation is a local source. Large-scale

FIG. 1 *a*, Vertical profiles of the global mean fractional change in specific humidity  $q$  for the last month of the GCM simulations; the difference is computed as the warmer (+2 K) minus the cooler (−2 K) perturbed SST climate. *b*, The corresponding profiles of the absolute change in relative humidity, obtained by averaging instantaneous values of  $r$  over the month. The associated mean upper-troposphere temperature change is 5.3 and 5.6 K in the old and new versions of the GCM, respectively. Note that for water vapour concentration in the upper troposphere to decrease as climate warms, as predicted by several authors<sup>3–5</sup>, relative humidity would have to decrease by more than 20%. Continuous trace, model II; dashed trace, new convection and clouds.



eddies transfer water vapour upwards from low altitudes, especially in mid-latitude storms where moist air rises near warm fronts and drier air sinks behind cold fronts. The same is true of the mean meridional circulation (MMC), dominated by the Hadley cell, whose rising branch is moist and sinking branch drier.

Our two simulations used the general circulation model (GCM) of the NASA/Goddard Institute for Space Studies. One used the standard version of the GCM, called model II<sup>9</sup>. Model II contains a penetrative cumulus scheme with representations of compensating subsidence, detrainment and evaporation of falling precipitation; the cumulus mass flux in unstable conditions is 50% of the mass of the cloud base layer. This differs from traditional convective adjustment<sup>10</sup> and cloud–environment mixing (Kuo-type)<sup>11</sup> schemes, which directly mix moisture upward. Stratiform clouds are diagnosed by assigning a temperature variance on scales smaller than that of the grid and computing the supersaturated fraction within each grid box.

The second simulation used a new version of the GCM with improved representations of cumulus<sup>12,13</sup> and stratiform cloud<sup>14</sup> based on recent tropical field studies and validated against a variety of satellite data sets; in other respects, this model is identical to model II. The new cumulus model includes computation of mass flux designed to produce a quasi-equilibrium<sup>15</sup> between convective-scale and large-scale motions, simultaneous deep and shallow convection, and transport by cumulus-scale

downdrafts as well as environmental subsidence. Calculations for stratiform clouds are based on a cloud liquid–ice water budget, including a representation of mesoscale cumulus anvils, different microphysical properties for liquid and ice, collection of cloud water by precipitation, diffusional growth of ice, cloud-top entrainment instability and variable optical thickness. Evaporation of condensate is largely restricted to the lower troposphere, beneath the bases of cumulus anvils, and this allows a more direct test of the effects of cumulus subsidence in the upper troposphere. Both models were run with  $8^\circ \times 10^\circ$  horizontal resolution and nine vertical levels, including three in the upper troposphere (layers centred at 201, 320 and 468 mbar).

The idealized simulation of climate change was identical to that conducted in a recent comparison of 19 GCMs<sup>16</sup>. Both models were perturbed with globally uniform −2 K and +2 K increments of sea surface temperature (SST), and the differences between the warmer and cooler climates compared. The models were run for one year as if conditions for July persisted throughout. Quantities of sea ice were fixed. Although this differs in several ways from GCM simulations of increasing trace gases, the changes in moisture budget that we describe are consistent with those in an experiment with model II that considered doubled carbon dioxide concentrations<sup>2</sup>.

Figure 1 shows the changes in specific and relative humidity profiles (warmer minus cooler) that occur in the two versions of the GCM. The concentration of water vapour increases substantially at all altitudes as the climate warms. The greatest fractional enhancement occurs in the upper troposphere, although the greatest absolute increase is near the surface. Relative humidity is almost constant in the lower troposphere and increases by a few per cent at higher levels. The new version of the GCM has slightly stronger water vapour feedback than Model II: a feedback analysis using a one-dimensional radiative–convective model<sup>2</sup> indicates that the humidity increases in Fig. 1 contribute 2.69 K to the warming in model II and 2.98 K in the new version of the GCM. The changes predicted by the two models are nonetheless strikingly similar, given the substantial differences in the physics employed. The small changes in  $r$  in both simulations imply that climate-induced changes in  $q$  are largely due to changes in  $q_s$ . This suggests that water vapour feedback is controlled primarily by temperature and is not very sensitive to the fine-tuning of the cloud models. Six other GCMs with mass-flux convection schemes also give strong positive water vapour feedback when subjected to the same SST perturbation<sup>16</sup>.

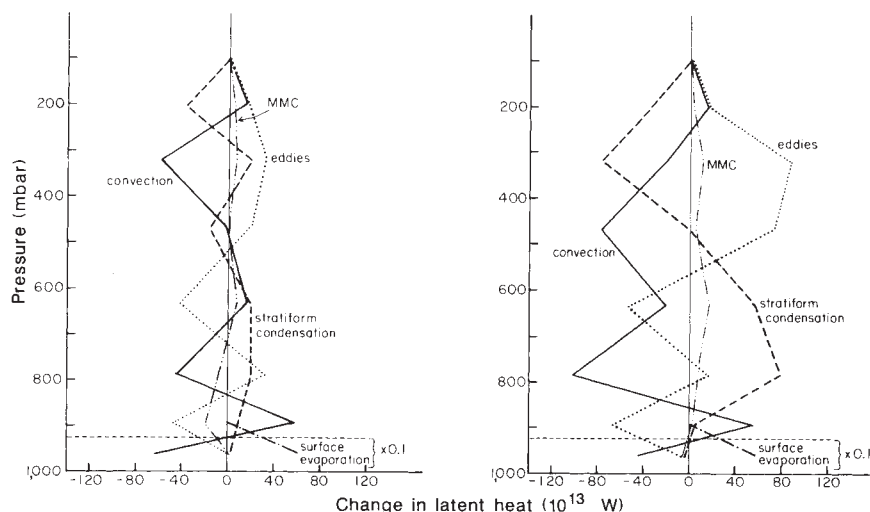
The reasons for positive water vapour feedback are made clear by examining changes in the individual terms of the atmospheric moisture budget between the warmer and cooler climate (Fig. 2). In equilibrium, there is no net moisture storage, so the

TABLE 1 Global diagnostics of general circulation strength and specific humidity gradient

	Model II		New convection and clouds	
	−2 K	+2 K	−2 K	+2 K
Cumulus mass flux ( $10^{11}$ kg s <sup>−1</sup> )	18.8	17.8	11.7	11.3
Eddy kinetic energy ( $10^4$ J m <sup>−2</sup> )	91.5	86.7	103.3	107.1
Peak Hadley cell streamfunction ( $10^9$ kg s <sup>−1</sup> )	184	172	156	160
Specific humidity difference 468 mbar – 201 mbar ( $10^{-4}$ kg per kg)	11.4	16.9	11.0	17.5
4°N – 59°N ( $10^{-4}$ kg per kg)	14.0	24.2	16.1	23.0

The numbers are for the final month of the simulations for both versions of the GCM. Convective moisture transport depends only on the vertical humidity gradient; transport by large-scale motions is affected by both horizontal and vertical gradients.

FIG. 2 Globally averaged vertical profiles of the changes (warmer minus cooler) in the individual components of the moisture budget (expressed in units of change of latent heat per unit time) for the last month of the GCM simulations for model II (left) and the new version of the GCM (right). The abscissa represents the climate change caused by each process in the time derivative of water vapour mass multiplied by the latent heat of condensation of water. The full lines represent both moist (cumulus clouds) and dry (primarily boundary layer turbulence) convection, almost exclusively moist above 600 mbars. The dotted lines include transient and stationary eddies, the tropical Walker circulation and the GCM representation of mesoscale cumulus updrafts and downdrafts. The MMC (dot-dashed lines) is dominated by the Hadley cell, with small contributions from the Ferrel and polar cells. The dashed lines represent stratiform condensation, including both sinks (cloud formation) and sources (evaporation of falling precipitation) of vapour resulting from phase changes. At the lowest model level, the abscissa has been multiplied by 0.1 so that, for example, a term in surface evaporation which is  $\sim 600 \times 10^{13} \text{ W}$  is plotted as  $\sim 60 \times 10^{13} \text{ W}$ .



net effect of the individual processes shown in Fig. 2 sum to zero at each level. A positive (negative) change in the figure means that the process in question moistens (dries) the warmer climate more than the cooler climate. In both versions of the GCM, cumulus-induced subsidence increases drying in the warmer climate at 320 and 468 mbar, as anticipated by Ellsaesser<sup>3</sup> and Lindzen<sup>4,5</sup>, but this is offset by increased moistening as a result of net upwards transport by large-scale eddies and the MMC. The eddies and MMC oppose convection because they converge moisture throughout the upper troposphere, whereas convection does so only at cloud top. A high proportion (roughly two-thirds according to model II, one-half according to the new version of the GCM) of the increased global eddy moistening at 320 mbar occurs outside the latitudes of tropical convection, much of it in mid-latitude storms. Global budgets therefore cannot be reliably inferred by considering tropical processes in isolation. At the tropopause, convection itself increasingly moistens the warmer atmosphere, because detrainment of saturated cloud air and ice occurs preferentially at higher altitude, and with increased condensate, as the climate warms.

Upper-troposphere humidity is maintained by transport of water down its gradient from lower to upper troposphere. Thus, upper-level water vapour increases in the GCM only if transports by the individual processes increase in the warmer climate. Dynamical moisture transport depends on the product of a mass flux (density times velocity) and the specific humidity gradient. Table 1 shows that the mass fluxes associated with various components of the general circulation change little, and sometimes decrease, as climate warms. The increased moisture transport is thus caused solely by marked increases in the vertical and horizontal humidity gradients, which are tightly coupled to temperature. In other words, upper-troposphere humidity increases in a warmer climate, because a general circulation that is almost unchanged will transport water upwards along a much steeper gradient.

Recent satellite data sets confirm the GCM view of water vapour feedback on climate. The SAGE II solar occultation instrument, for example, indicates that water vapour concentration is higher in summer than winter in both hemispheres at all tropospheric altitudes and latitudes, regardless of whether the comparison is made at a location of rising or sinking in the MMC<sup>6</sup>. Seasonal differences in relative humidity measured by SAGE II are largest in the upper troposphere (typically 5–10% higher in summer), consistent with the predictions of the GCM. Longwave radiation fluxes measured in clear-sky regions by the

Earth Radiation Budget Experiment imply that the contribution of water vapour to the greenhouse effect is largest in the warmest ocean regions, regardless of its vertical distribution<sup>7</sup>. Finally, radiosonde moisture profiles indicate higher amounts of water vapour both in summer and in the warm phase of the El Niño cycle in the middle and upper troposphere<sup>17,18</sup>, although the uncertainty in specific humidity at these altitudes is considerable. In summary, the available observations indicate higher upper-troposphere humidity in a warmer atmosphere, the opposite result to that expected from consideration of cumulus subsidence alone.

Our findings have several implications for climate monitoring strategies and global warming policy. As water vapour produces the largest known positive feedback on climate, it is essential to refine our estimates of its impact by making more accurate observations of upper-troposphere water vapour and radiative fluxes. The large increases in humidity seen in Fig. 1 also indicate that long-term monitoring of water vapour by satellites may be a useful means of detecting a global warming trend<sup>19</sup>. The general agreement between GCM and observational estimates of water vapour feedback also gives us an estimate of the minimum climate sensitivity to human activity. Specifically, an equivalent doubling of CO<sub>2</sub> can be expected to produce an equilibrium global warming of at least 1.5–2.0 °C (using the most negative estimate of cloud feedback produced by a GCM<sup>20</sup>), even more if cloud and snow or ice feedbacks are nearly neutral or positive. □

Received 28 January; accepted 11 April 1991.

1. Manabe, S. & Wetherald, R. T. *J. Atmos. Sci.* **24**, 241–259 (1967).
2. Hansen, J. et al. *Climate Processes and Climate Sensitivity* (eds Hansen, J. & Takahashi, T.), 130–163 (American Geophysical Union, Washington DC, 1984).
3. Ellsaesser, H. W. *Atmos. Environ.* **18**, 431–434 (1984).
4. Lindzen, R. S. *Bull. Am. Met. Soc.* **71**, 288–299 (1990).
5. Lindzen, R. S. *Bull. Am. Met. Soc.* **71**, 1465–1467 (1990).
6. Rind, D. et al. *Nature* **349**, 500–503 (1991).
7. Raval, A. & Ramanathan, V. *Nature* **342**, 758–761 (1989).
8. Wallace, J. M. & Hobbs, P. V. *Atmospheric Science—An Introductory Survey* (Academic, New York, 1977).
9. Hansen, J. et al. *Mon. Weath. Rev.* **111**, 609–662 (1983).
10. Manabe, S. et al. *Mon. Weath. Rev.* **93**, 769–798 (1965).
11. Kuo, H. L. *J. Atmos. Sci.* **31**, 1232–1240 (1974).
12. Del Genio, A. D. & Yao, M.-S. *J. Atmos. Sci.* **45**, 2641–2668 (1988).
13. Yao, M.-S. & Del Genio, A. D. *J. Clim.* **2**, 850–863 (1989).
14. Del Genio, A. D. & Yao, M.-S. *AMS Conf. Cloud Phys. Preprint No. 9A.4*, 497–504 (American Meteorological Society, Boston, 1990).
15. Arakawa, A. & Chen, J.-M. *Short- and Medium-Range Numerical Weather Prediction*, Suppl. to *J. Met. Soc. Japan*, 107–131 (1987).
16. Cess, R. D. et al. *J. Geophys. Res.* **95**, 16601–16615 (1990).
17. Oort, A. H. *NOAA Prof. Paper No. 14* (US Dept. Commerce, Washington DC, 1983).
18. Pan, Y.-H. & Oort, A. H. *Mon. Weath. Rev.* **111**, 1244–1258 (1983).



19. Hansen, J., Rossow, W. & Fung, I. *Issues Sci. Tech.* **7**, 62–69 (1990).  
 20. Mitchell, J. F. B. *et al. Nature* **341**, 132–134 (1989).

ACKNOWLEDGEMENTS. We thank R. Cess, J. Hansen, R. Miller, W. Rossow, D. Starr, P. Stone and M.-S. Yao for helpful comments. This work was supported by the DOE Interagency Agreements under the Quantitative Links and Atmospheric Radiation Measurement Programs. R.A.R. is supported by ST Systems Corporation through a support contract with NASA.

## Enhanced particle fluxes in Bay of Bengal induced by injection of fresh water

V. Ittekkot\*, R. R. Nair†, S. Honjo‡, V. Ramaswamy†, M. Bartsch\*, S. Manganini‡ & B. N. Desai†

\* Institute of Biogeochemistry and Marine Chemistry, University of Hamburg, Bundesstrasse 55, 2000 Hamburg 13, Germany  
 † National Institute of Oceanography, Dona Paula, Goa 403004, India  
 ‡ Woods Hole Oceanographic Institution, Woods Hole, Massachusetts 02543, USA

THE melting of ice sheets during deglaciation results in the injection of large amounts of fresh water into the oceans<sup>1</sup>. To investigate how such injections might influence particle fluxes in the ocean, and hence the uptake of atmospheric CO<sub>2</sub>, we deployed three sediment-trap moorings (two traps in each mooring) in the northern, central and southern parts of the Bay of Bengal, respectively. The Bay of Bengal is suitable for such a study, because some of the world's largest rivers<sup>2</sup> supply pulses of fresh water and sediment to the bay, resulting in large seasonal changes in surface salinity<sup>3</sup>. We find that the maximum river discharge, which occurs during the southwest monsoon, coincides with the maximum observed flux of particulate matter. From north to south, the carbonate flux increases, whereas fluxes of opal, organic carbon and particulate matter decrease. The overall flux pattern seems to be controlled by the seasonally varying input from the rivers and the accompanying shift in marine biogenic production. We conclude that freshwater pulses during deglaciation may therefore have caused similar

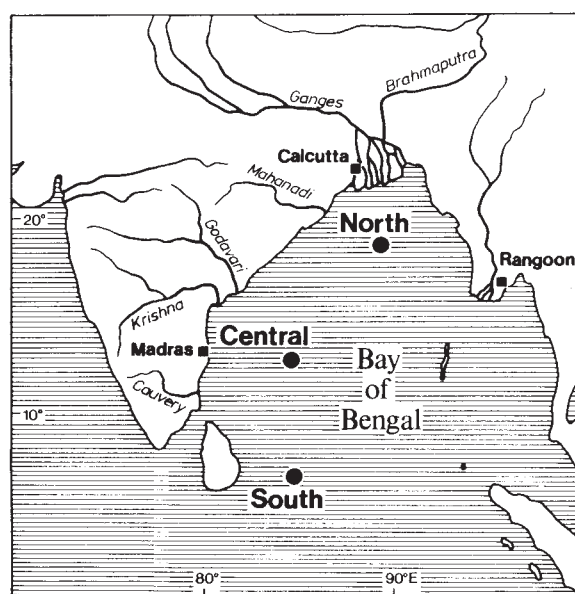


FIG. 1 Locations of sediment-trap moorings in the northern (17°26'N, 89°35'E; water depth 2,263 m, trap depths 809 and 1,727 m), central (13°09'N, 84°21'E; water depth 3,259 m, trap depths 906 and 2,282 m) and southern (04°26'N, 87°19'E; water depth 4,017 m, trap depths 1,040 and 3,006 m) Bay of Bengal. Each mooring consists of two time-series sediment traps<sup>17</sup>. They were first deployed in October 1987 and have been recovered and redeployed three times since October 1987 using the research vessels RV *Sonne* and ORV *Sagar Kanya*.

shifts in marine biogenic production, resulting in short-term episodes of increased oceanic uptake of atmospheric CO<sub>2</sub>.

Surface salinity in the Bay of Bengal fluctuates over a wide range of values, both seasonally and geographically<sup>4</sup>. The greatest change occurs towards the end of the southwest monsoon, when water discharge from the Ganges and Brahmaputra and from the peninsular Indian rivers is at a maximum. During this period (August–November) mean salinity decreases by more than 7‰ (ref. 4).

The results from the first year of our continuing experiment in the Bay of Bengal show seasonal fluctuations in particle fluxes at all three sites (Figs 1 and 2). Forty to fifty per cent of the total annual flux occurs during the southwest monsoon, which covers 3–4 months. During the rest of the year (northeast monsoon and intermonsoon periods), particle fluxes are uniformly low. An exception is one sampling interval during

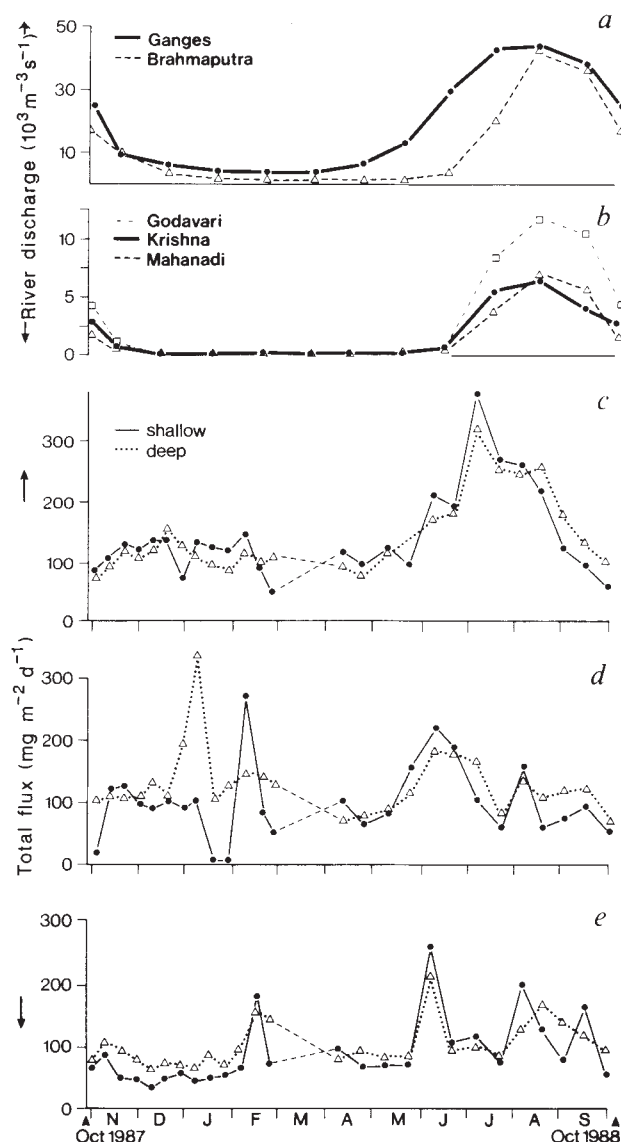


FIG. 2 Time-series data of particle flux in the Bay of Bengal for October 1987 to October 1988. *a, b*, River discharge data from ref. 18. *c, d, e*, Total particle flux from north, central and south Bay of Bengal, respectively. The sediment traps were programmed to measure the flux of sinking particles at intervals of 9.5 days during the first deployment and 14.5 days during the second deployment. The collecting cups were poisoned with mercury chloride before deployment. On recovery of the traps, the samples were wet-sieved and split using a precision rotary splitter. One-quarter of the <1-mm size fraction was filtered through preweighed Nuclepore filters (0.5 µm) and dried at 40 °C. This fraction was used for total flux calculations.